Differential electron emission in the ionization of Ne and Xe atoms under fast bare carbon ion impact

2015 J. Phys. B: At. Mol. Opt. Phys. 48 115206

(http://iopscience.iop.org/0953-4075/48/11/115206)

IOP Publishing Journal of Physics B: Atomic, Molecular and Optical Physics

J. Phys. B: At. Mol. Opt. Phys. **48** (2015) 115206 (15pp) doi:10.1088/0953-4075/48/11/115206

Differential electron emission in the ionization of Ne and Xe atoms under fast bare carbon ion impact

Shubhadeep Biswas[1], **J M Monti**[2], **C A Tachino**[2], **R D Rivarola**[2] and **L C Tribedi**[1]

[1] Tata Institute of Fundamental Research, Homi Bhabha Road, Colaba, Mumbai 400 005, India
[2] Laboratorio de Colisiones Atómicas, Facultad de Ciencias Exactas, Ingeniería y Agrimensura, and Instituto de Física Rosario (CONICET-UNR), 2000 Rosario, Argentina

E-mail: shubhadeep@tifr.res.in, and lokesh@tifr.res.in

Received 5 January 2015, revised 12 March 2015
Accepted for publication 27 March 2015
Published 28 April 2015

Abstract

Measurement of the energy and angular distributions of the double differential cross section (DDCS) of electron emission from Ne and Xe atoms in collision with 5 MeV u^{-1} bare carbon ions is reported. This study aimed to investigate the electron emission processes in the case of multi-electronic systems. In general, several clear differences between the electron emission spectra of Ne and Xe are found, which indicate the influence of the increasing number of electrons. For instance, the sharp peak due to the binary nature of collision is almost absent in the case of Xe, unlike Ne, which could be understood due to the increasing contribution from the strongly bound inner shell (such as 4*d*) electrons for the Xe atom. The forward–backward angular asymmetry has also been derived from the angular distributions. For Xe, the qualitative behaviour of the asymmetry parameter is seen to be quite different since it reveals structures due to Auger contributions. It is, in general, different and much lower than that for Ne, which shows the smooth behaviour that one finds for other lighter atoms like He. The single differential and total cross sections are also derived. The theoretical calculations based on the *prior* form of the continuum distorted wave-eikonal initial state (CDW-EIS) approximation have been provided for both the targets. Overall, it gives a very good agreement with the energy and the angular distributions of DDCS for Ne. For Xe, the agreement is not as good as for Ne. We also provide a detailed discussion on the DDCS obtained from different sub-shell ionization, estimated in this framework.

Keywords: multi-electron atoms, ionization, electron emission, double differential distributions, heavy ion projectile, ion-atom collisions, experiment

1. Introduction

Collision with charged particles has traditionally been used to explore different aspects of atomic and molecular physics for several decades. Electrons as well as low and highly charged ions are used for this purpose as a projectile. One of the main motivations behind these studies is complete understanding of the basic fundamental collision mechanisms at a microscopic level. In this regard, in most of the cases, smaller atomic [1–8] or molecular [6, 9–13] targets which contain one or two electrons were used as the subject of study, simply to avoid further complexities which increase with the increasing number of particles involved. There is some literature available which involves larger targets, but mainly for investigating some specific physics interests like the interference effect [14, 15], collective excitation of electrons in molecules [16], etc. Not much detailed systematic effort has been devoted to addressing the fundamental issues regarding collision with large multi-electronic targets. Apart from their fundamental importance, these studies are useful to other diverse fields such as atmospheric physics, plasma physics, medical physics or astrophysics. Understanding at a simple

atomic or molecular level can be regarded as the first step of exploration of these subjects where species with large numbers of electrons are involved. Furthermore, some of these subjects, like heavy ion therapy, are directly related to the physics of ion collision with multi-electronic systems [17–21].

As a tool of investigation, the study of differential electron emission can give adequate insight into different ionization mechanisms and it is also well known that the double differential cross section (DDCS) of electron emission can also provide a stringent test to the theoretical models compared to the total ionization cross section (TCS). In this context, it is worth mentioning that different perturbative quantum mechanical models were checked thoroughly for the one or two electron systems [8, 22–25]. It turns out that for highly charged ion collision, the reaction dynamics is generally well reproduced by a state-of-the-art model such as the continuum distorted wave-eikonal initial state (CDW-EIS) approximation [22, 26]. This model efficiently incorporates the post collision projectile influence on the ionized active electron. Further, from some of the recent communications, it has been established that the *prior* form of the model gives an appropriate description of experiments, particularly for the cases where the multi-electronic description of the target is needed [27–29]. But this has been checked for few-electron systems. For large systems it has been yet to be verified. In these cases, additional difficulties come from the large number of residual electrons residing on the target atom. These would certainly influence the evolution of the ionized electron. Other than that, inner shell processes play an important role in the ionization processes of these large systems. There are plenty of studies on inner shell ionization using x-ray techniques [30, 31], or on inner shell electron capture [32, 33] and the Auger channel, which confirm the fact.

To address these issues, an appreciable number of data sets are required involving large multi-electronic targets. But, to the best of our knowledge, there are very few data sets available which provide the differential electron emission cross section in a wide energy and angular range, under highly charged ion impact. In this report we provide the absolute DDCS of electron emission in the ionization of Ne and Xe atoms under 5 MeV u^{-1} bare C ion impact. The existing electron spectroscopic data for Ne mainly involve low energy low charge state ions [29, 34–41]. On the other hand for Xe, not much experimental data exist, the only available data set involves neutral atoms as the projectile [42]. In that sense, the present data sets are an important inclusion to the literature. Other than that, the comparison between the electron emission spectra corresponding to the above-mentioned targets clearly indicates the differences which occur due to the increasing number of target electrons. In addition to the experimental measurements, we also provide theoretical calculations based on the *prior* form of the CDW-EIS model for both the targets. It is worth noting that, as these systems involve high velocity ions ($v \backsim 14$ a.u.), ionization is the most dominant process in these cases. Electron capture has a very low cross section at such high energy. Therefore, these systems would be appropriate for verification of the model. Furthermore, in addition to the total DDCS, we also discuss, in detail, the contributions from different sub-shells to the total DDCS.

The paper is organized as follows. In section 2, an overview of the experimental technique and the possible uncertainties in the measurements are described briefly. Section 3 provides the necessary details of the theoretical model used for both the targets. A comparative discussion of the present results is given in section 4. It is divided in four subsections, the first two (4.1 and 4.2) describe the energy distribution of the DDCS at different emission angles and the angular distribution of the DDCS at different ejected electron energy, respectively. The next subsection (4.3) sheds light on the forward–backward angular asymmetry in the electron distribution. In the last subsection (4.4), the comparison at the single differential cross section (SDCS) level is highlighted. In section 5, a summary of the work is presented. In addition to that, some of the representative absolute DDCS and SDCS values, for both the Ne and the Xe targets, are provided in tables 1 and 2, respectively.

2. Overview of the experiment

The experiment was carried out with the 5 MeV u^{-1} C^{6+} ion beam available from the 14 MV Pelletron accelerator facility at TIFR, Mumbai, India. The highly collimated beam was passed through a scattering chamber whose base vacuum was obtained better than 2×10^{-7} Torr. The number of projectile ions was determined by detecting them with a Faraday cup. During interaction with the target gases, the scattering chamber was flooded at a pressure of 0.15 mTorr. The background was measured by collecting the emitted electrons in 'without gas' conditions with the ion beam on. A hemispherical electrostatic analyser with 6% [43] energy resolution was used to energy analyse the emitted electrons and a channel electron multiplier (CEM) was used to detect them. With the help of a motorized turn table, the spectrometer is rotated to detect the electrons emitted at different angles. From the electron count at particular energy and emission angles, and by subtracting the background contribution, the DDCS was obtained from the first principle. In this experiment we have detected the electrons of energy within the range of 1–1000 eV for Ne and 1–600 eV for Xe. The energy dependence of the DDCS was investigated at 12 different angles, namely 20°, 30°, 45°, 60°, 75°, 80°, 90°, 105°, 120°, 135°, 150° and 160°. Further details of the experimental technique is available in [43]. In these measurements, in general, the error due to the statistical fluctuations was low. For the Xe target, the maximum statistical uncertainty was always less than 5% throughout the entire experiment. For the Ne target, similar figures were obtained for forward angle measurements and low energy backward angle measurements. In the high energy part ($\gtrsim$850 eV), it increased to about 20%. Other than that the gas pressure fluctuation mainly contributes about 6% to 7% to the total absolute error. The remaining systematic uncertainties together contribute a very small

Table 1. Measured double differential cross sections for Ne in units of Mb(eV sr)$^{-1}$ at different angles. The last column displays the $\frac{d\sigma}{d\epsilon_e}$ values in units of Mb eV^{-1}. The last row displays the $\frac{d\sigma}{d\Omega_e}$ values in units of Mb sr^{-1}. For errors, see the text.

ϵ_e(eV)	20°	30°	45°	60°	75°	80°	90°	105°	120°	135°	150°	160°	$\frac{d\sigma}{d\epsilon_e}$
1	3.78E0	3.80E0	3.50E0	3.36E0	3.26E0	3.18E0	3.13E0	3.19E0	2.77E0	2.64E0	2.50E0	2.36E0	3.67E1
3	2.89E0	2.85E0	2.80E0	2.70E0	2.63E0	2.55E0	2.48E0	2.63E0	2.18E0	2.07E0	1.97E0	1.62E0	2.92E1
5	2.25E0	2.36E0	2.23E0	2.28E0	2.15E0	2.12E0	1.99E0	2.18E0	1.80E0	1.69E0	1.62E0	1.23E0	2.39E1
7	1.84E0	1.94E0	1.84E0	2.01E0	1.86E0	1.84E0	1.65E0	1.78E0	1.45E0	1.38E0	1.28E0	9.88E-1	1.99E1
9	1.53E0	1.62E0	1.55E0	1.69E0	1.58E0	1.63E0	1.34E0	1.46E0	1.15E0	1.08E0	1.02E0	8.10E-1	1.65E1
13	1.13E0	1.24E0	1.14E0	1.28E0	1.22E0	1.21E0	9.90E-1	1.04E0	8.31E-1	7.46E-1	6.85E-1	5.54E-1	1.21E1
17	8.09E-1	8.81E-1	8.62E-1	9.77E-1	9.36E-1	9.20E-1	7.98E-1	7.99E-1	6.16E-1	5.54E-1	4.91E-1	3.83E-1	9.18E0
20	8.15E-1	7.29E-1	7.34E-1	7.99E-1	8.24E-1	7.99E-1	7.68E-1	6.80E-1	5.41E-1	4.89E-1	3.97E-1	3.74E-1	7.98E0
30	5.03E-1	4.98E-1	5.18E-1	5.46E-1	5.65E-1	5.46E-1	5.14E-1	4.48E-1	3.55E-1	3.00E-1	2.45E-1	2.12E-1	5.33E0
40	3.72E-1	3.80E-1	3.67E-1	3.87E-1	4.09E-1	3.97E-1	3.75E-1	3.19E-1	2.33E-1	1.99E-1	1.54E-1	1.35E-1	3.78E0
50	2.80E-1	2.71E-1	2.67E-1	2.87E-1	3.15E-1	3.00E-1	2.96E-1	2.26E-1	1.64E-1	1.31E-1	1.06E-1	9.09E-2	2.77E0
70	1.61E-1	1.61E-1	1.49E-1	1.81E-1	1.99E-1	1.84E-1	1.84E-1	1.36E-1	8.37E-2	6.38E-2	5.46E-2	4.44E-2	1.64E0
90	1.04E-1	1.07E-1	1.01E-1	1.26E-1	1.29E-1	1.32E-1	1.23E-1	8.22E-2	4.56E-2	3.62E-2	2.90E-2	2.30E-2	1.06E0
110	7.47E-2	7.45E-2	7.14E-2	9.14E-2	9.54E-2	9.08E-2	8.91E-2	5.48E-2	2.96E-2	2.16E-2	1.87E-2	1.31E-2	7.44E-1
130	5.24E-2	5.30E-2	5.04E-2	6.16E-2	7.59E-2	7.04E-2	6.60E-2	3.46E-2	1.98E-2	1.39E-2	1.17E-2	8.52E-3	5.30E-1
160	3.25E-2	3.29E-2	3.16E-2	3.97E-2	5.37E-2	5.58E-2	4.30E-2	2.03E- 2	1.16E-2	7.19E-3	5.85E-3	4.43E-3	3.45E-1
200	2.02E-2	2.00E-2	2.02E-2	2.35E-2	3.51E-2	4.19E-2	2.92E-2	1.22E-2	7.03E-3	3.60E-3	3.27E-3	2.63E-3	2.22E-1
240	1.38E-2	1.29E-2	1.29E-2	1.68E-2	2.60E-2	3.12E-2	1.99E-2	7.58E-3	3.85E-3	1.84E-3	2.04E-3	1.48E-3	1.47E-1
280	1.04E-2	9.61E-3	9.52E-3	1.16E-2	1.89E-2	2.36E-2	1.42E-2	4.58E-3	2.31E-3	1.30E-3	1.35E-3	1.02E-3	1.08E-1
320	6.93E-3	7.10E-3	6.47E-3	9.17E-3	1.61E-2	1.92E-2	1.17E-2	3.26E-3	1.45E-3	9.66E-4	9.60E-4	8.03E-4	8.17E-2
360	5.96E-3	5.19E-3	5.62E-3	6.86E-3	1.32E-2	1.50E-2	8.43E-3	2.14E-3	1.24E-3	5.81E-4	6.54E-4	4.68E-4	6.51E-2
400	5.15E-3	4.34E-3	3.80E-3	5.43E-3	1.14E-2	1.28E-2	6.53E-3	1.65E-3	9.19E-4	4.07E-4	4.68E-4	4.26E-4	5.15E-2
440	3.77E-3	3.40E-3	2.99E-3	4.35E-3	8.76E-3	1.14E-2	5.24E-3	1.28E-3	6.31E-4	3.47E-4	3.78E-4	2.86E-4	4.20E-2
480	3.26E-3	2.98E-3	2.82E-3	3.84E-3	8.54E-3	9.47E-3	4.00E-3	9.71E-4	5.40E-4	1.89E-4	2.90E-4	2.29E-4	3.64E-2
520	2.89E-3	2.57E-3	1.90E-3	3.43E-3	6.62E-3	8.37E-3	3.34E-3	8.35E-4	3.57E-4	1.65E-4	1.97E-4	1.60E-4	2.94E-2
560	2.20E-3	2.05E-3	1.87E-3	2.55E-3	6.74E-3	7.71E-3	2.71E-3	6.49E-4	2.79E-4	1.70E-4	2.12E-4	1.47E-4	2.65E-2
600	1.83E-3	1.74E-3	1.82E-3	2.32E-3	5.97E-3	6.99E-3	1.98E-3	4.22E-4	2.48E-4	1.70E-4	2.17E-4	1.41E-4	2.30E-2
$\frac{d\sigma}{d\Omega_e}$	6.05E1	6.09E1	5.88E1	6.47E1	6.93E1	6.89E1	6.00E1	5.16E1	3.94E1	3.47E1	3.08E1	2.54E1	

Table 2. Measured double differential cross sections for Xe in units of Mb(eV sr)$^{-1}$ at different angles. The last column displays the $\frac{d\sigma}{d\epsilon_e}$ values in units of Mb eV^{-1}. The last row displays the $\frac{d\sigma}{d\Omega_e}$ values in units of Mb sr^{-1}. For errors, see the text.

ϵ_e(eV)	20°	30°	45°	60°	75°	80°	90°	105°	120°	135°	150°	160°	$\frac{d\sigma}{d\epsilon_e}$
1	1.78E1	2.00E1	1.67E1	1.35E1	1.35E1	1.19E1	1.06E1	1.07E1	1.19E1	1.18E1	9.99E0	9.50E0	1.50E2
3	1.36E1	1.55E1	1.31E1	9.70E0	1.00E0	8.88E0	8.09E0	7.93E0	9.50E0	9.14E0	7.68E0	6.93E0	1.14E2
5	1.04E1	1.20E1	1.02E1	7.22E0	7.93E0	6.89E0	6.42E0	6.74E0	7.56E0	6.77E0	6.20E0	5.40E0	8.97E1
7	8.32E0	8.80E0	7.96E0	5.89E0	6.45E0	5.67E0	5.26E0	5.64E0	5.71E0	4.89E0	4.40E0	3.98E0	7.04E1
9	6.65E0	6.49E0	6.13E0	4.92E0	5.45E0	4.77E0	4.31E0	4.52E0	4.34E0	3.65E0	3.18E0	2.96E0	5.57E1
13	3.39E0	3.42E0	3.39E0	3.18E0	3.34E0	3.08E0	2.76E0	2.60E0	2.36E0	1.89E0	1.75E0	1.65E0	3.24E1
16	2.38E0	2.42E0	2.35E0	2.10E0	2.45E0	2.15E0	2.08E0	2.28E0	1.74E0	1.43E0	1.52E0	1.32E0	2.41E1
20	1.47E0	1.51E0	1.50E0	1.56E0	1.64E0	1.50E0	1.47E0	1.53E0	1.11E0	9.40E-1	9.72E-1	8.81E-1	1.62E1
24	1.28E0	1.37E0	1.34E0	1.40E0	1.54E0	1.40E0	1.31E0	1.32E0	9.74E-1	8.09E-1	8.52E-1	7.78E-1	1.44E1
28	1.07E0	1.15E0	1.15E0	1.19E0	1.33E0	1.22E0	1.19E0	1.17E0	8.94E-1	6.88E-1	7.32E-1	6.74E-1	1.26E1
32	1.22E0	1.28E0	1.27E0	1.30E0	1.46E0	1.30E0	1.25E0	1.28E0	1.02E0	1.00E0	8.80E-1	7.82E-1	1.42E1
36	7.84E-1	8.25E-1	8.21E-1	8.80E-1	1.01E0	9.52E-1	8.79E-1	7.03E-1	6.28E-1	6.00E-1	5.26E-1	5.31E-1	9.14E0
40	6.33E-1	6.42E-1	6.31E-1	6.98E-1	8.73E-1	7.68E-1	7.43E-1	6.24E-1	4.70E-1	4.50E-1	3.86E-1	3.82E-1	7.37E0
50	4.55E-1	4.60E-1	4.48E-1	4.84E-1	6.91E-1	5.73E-1	5.47E-1	4.45E-1	3.29E-1	3.06E-1	2.61E-1	2.50E-1	5.32E0
60	2.90E-1	2.87E-1	2.77E-1	3.11E-1	4.76E-1	3.96E-1	3.76E-1	2.72E-1	2.01E-1	1.79E-1	1.49E-1	1.44E-1	3.41E0
80	1.61E-1	1.92E-1	1.48E-1	1.70E-1	2.76E-1	2.40E-1	2.56E-1	1.38E-1	9.49E-2	7.75E-2	6.18E-2	6.23E-2	1.91E0
100	1.09E- 1	1.13E-1	1.00E-1	1.16E-1	2.03E-1	1.75E-1	1.81E-1	8.06E-2	5.88E-2	5.00E-2	3.96E-2	3.79E-2	1.29E0
120	8.49E-2	8.27E-2	7.90E-2	9.17E-2	1.54E-1	1.41E-1	1.30E-1	5.73E-2	4.38E-2	3.67E-2	3.42E-2	3.04E-2	9.84E-1
140	6.73E-2	7.01E-2	6.69E-2	7.14E-2	1.31E-1	1.16E-1	1.08E-1	4.38E-2	3.29E-2	2.98E-2	2.86E-2	2.64E-2	7.98E-1
160	5.64E-2	6.02E-2	5.82E-2	6.00E-2	1.01E-1	9.10E-2	8.63E-2	3.47E-2	2.65E-2	2.55E-2	2.61E-2	2.20E-2	6.49E-1
200	3.57E-2	4.30E-2	4.19E-2	4.52E-2	7.93E-2	6.89E-2	5.84E-2	2.53E-2	2.10E-2	1.78E-2	1.69E-2	1.59E-2	4.74E-1
220	3.08E-2	4.01E-2	3.92E-2	3.95E-2	6.97E-2	6.13E-2	4.84E-2	2.18E-2	1.85E-2	1.51E-2	1.50E-2	1.61E-2	4.17E-1
240	2.80E-2	3.55E-2	3.55E-2	3.43E-2	6.85E-2	5.48E-2	4.02E-2	1.93E-2	1.69E-2	1.34E-2	1.36E-2	1.44E-2	3.74E-1
280	2.23E-2	2.93E-2	3.04E-2	3.02E-2	5.68E-2	4.75E-2	3.34E-2	1.83E-2	1.34E-2	1.19E-2	1.18E-2	1.23E-2	3.20E-1
320	1.92E-2	2.57E-2	2.85E-2	2.87E-2	5.00E-2	3.96E-2	2.68E-2	1.58E-2	1.26E-2	9.94E-3	1.10E-2	1.01E-2	2.81E-1
360	1.82E-2	2.30E-2	2.58E-2	2.79E-2	4.42E-2	3.55E-2	2.39E-2	1.50E-2	1.12E-2	9.81E-3	1.03E-2	8.70E-3	2.57E-1
400	1.59E-2	2.05E-2	2.28E-2	2.46E-2	4.04E-2	3.13E-2	2.05E-2	1.27E-2	1.07E-2	9.42E-3	1.05E-2	8.21E-3	2.30E-1
440	1.37E-2	1.77E-2	2.03E-2	2.17E-2	3.62E-2	2.97E-2	1.75E-2	1.09E-2	8.92E-3	7.64E-3	8.27E-3	8.48E-3	2.02E-1
480	1.43E-2	1.91E-2	1.99E-2	2.10E-2	3.42E-2	2.75E-2	1.71E-2	1.10E-2	1.14E-2	8.87E-3	9.09E-3	7.03E-3	2.02E-1
520	1.06E-2	1.27E-2	1.51E-2	1.78E-2	2.76E-2	2.20E-2	1.25E-2	7.58E-3	7.04E-3	5.27E-3	5.64E-3	4.44E-3	1.51E-1
560	7.52E-3	9.56E-3	1.02E-2	1.34E-2	1.60E-2	1.77E-2	7.61E-3	4.74E-3	3.90E-3	3.23E-3	3.24E-3	3.21E-3	1.00E-1
600	5.88E-3	6.91E-3	9.23E-3	1.14E-2	1.35E-2	1.41E-2	6.72E-3	3.30E-3	2.91E-3	2.11E-3	2.29E-3	2.43E-3	8.16E-2
$\frac{d\sigma}{d\Omega_e}$	1.75E2	1.75E2	1.74E2	1.68E2	1.81E2	1.60E2	1.46E2	1.32E2	1.22E2	1.09E2	9.87E1	9.06E1	

amount, which mainly arises from observation angle and solid angle measurements.

3. Theoretical model

Let us consider the single ionization reaction of a multi-electronic atom. The incident particle is a bare ion of charge Z_P that impinges on the atomic target with velocity $\vec{v}$ parallel to the z-axis of a laboratory reference frame located at the target nucleus. The treatment of the multi-electronic problem is solved by reducing it to the analysis of a one-electron system in which the passive electrons (the non-ionized ones) are considered to remain frozen in their initial orbitals during the collision and that the active electron (the emitted one) evolves independently of them in an effective Coulomb field of the residual target [22].

Double differential cross sections as a function of the energy ε_k and the solid angle Ω_k of the emitted electron can be defined as follows:

$$\sigma^{(2)}(\varepsilon_k, \theta_k) = \frac{\mathrm{d}\sigma}{d\varepsilon_k \, \mathrm{d}\Omega_k} = k \int \mathrm{d}\vec{\rho} \; \left| a_{i,f}^{-}(\vec{\rho}) \right|^2, \tag{1}$$

where the sign—refers to the *prior* version of the transition amplitude $a_{i,f}(\vec{\rho})$, $\vec{k}$ is the momentum of the electron, and $\vec{\rho}$ is the impact parameter vector. Introducing the two-dimensional Fourier transform of $a_{i,f}^{-}(\vec{\rho})$:

$$\mathcal{R}_{i,f}^{-}(\vec{\eta}) = \frac{1}{2\pi} \int \mathrm{d}\vec{\eta} \; \exp(i \, \vec{\eta} \cdot \vec{\rho}) \, a_{i,f}^{-}(\vec{\rho}), \tag{2}$$

which depends on the transverse momentum transfer $\vec{\eta}$, and employing Parseval's theorem [26], double differential cross sections can be also calculated as:

$$\sigma^{(2)}(\varepsilon_k, \theta_k) = k \int \mathrm{d}\vec{\eta} \; \left| \mathcal{R}_{i,f}^{-}(\vec{\eta}) \right|^2. \tag{3}$$

Into the straight line version of the impact parameter approximation and within the distorted wave model, the first order approximation for the *prior* version of the transition amplitude for the active electron may be written as:

$$a_{i,f}^{-}(\vec{\rho}) = \int_{-\infty}^{+\infty} \mathrm{d}t \left\langle \chi_f^{-} \left| W_i \right| \chi_i^{+} \right\rangle \tag{4}$$

where χ_i^{+} (χ_f^{-}) represents a distorted wavefunction that satisfies correct outgoing (incoming) asymptotic boundary conditions, and W_i is the perturbative operator acting on the entry channel in the continuum distorted wave-eikonal initial state (CDW-EIS) approximation [26]. This version is shown to correctly include the interaction between the active electron and the passive ones, whilst, in the *post* version this interaction is only partially included (see [27, 29]). Therefore χ_i^{+} and χ_f^{-} are chosen as:

$$\chi_i^{+,EIS}(\vec{r}, t) = \varphi_i(\vec{r}) \exp(-i\varepsilon_i t) \mathcal{L}_i^{+,EIS}(\vec{s}) \tag{5}$$

$$\chi_f^{-,CDW}(\vec{r}, t) = \varphi_k(\vec{r}) \exp(-i\varepsilon_k t) \mathcal{L}_f^{-,CDW}(\vec{s}), \tag{6}$$

with φ_i (φ_k) the bound (continuum) wavefunction of the active electron, and $\varepsilon_k = k^2/2$. Also, in the preceding expressions, $\vec{r}$ is the electron coordinate with respect to the origin of the laboratory reference frame, and $\vec{s}$ is the electron position vector with respect to the projectile nucleus. The eikonal and continuum distortion factors are given by the expressions:

$$\mathcal{L}_i^{+,EIS}(\vec{s}) = \exp\left[-i\nu \, \ln\left(vs + \vec{v} \cdot \vec{s} \right) \right] \tag{7}$$

$$\mathcal{L}_f^{-,CDW}(\vec{s}) = N(\varsigma) {}_1F_1\left[-i\varsigma; \, 1; \, -i\left(ps + \vec{p} \cdot \vec{s} \right) \right], \tag{8}$$

respectively, where $\nu = Z_P/v$, $\varsigma = Z_P/p$ with $\vec{p} = \vec{k} - \vec{v}$ the momentum of the electron considered with respect to a reference frame centred on the projectile nucleus which is moving with velocity $\vec{v}$, and $N(a) = \exp(a\pi/2)\Gamma(1 + i\,a)$, with ${}_1F_1(b; c; z)$ the Kummer confluent hypergeometric function. Therefore, the W_i operator in equation (4) gives:

$$\begin{aligned} W_i \, \chi_i^{+,EIS}(\vec{r}, t) = \varphi_i(\vec{r}) \exp(-i\varepsilon_i t) \\ \times \left[\frac{1}{2} \nabla_{\vec{s}}^2 \, \mathcal{L}_i^{+,EIS}(\vec{s}) \right. \\ \left. + \, \vec{\nabla}_{\vec{r}} \ln \varphi_i(\vec{r}) \cdot \vec{\nabla}_{\vec{s}} \mathcal{L}_i^{+,EIS}(\vec{s}) \right]. \end{aligned} \tag{9}$$

In this paper, initial bound orbitals are described by Roothaan–Hartree–Fock (RHF) wavefunctions [44]. The continuum state of the emitted electron in the residual target field is written as:

$$\begin{aligned} \varphi_k(\vec{r}) = (2\pi)^{-3/2} \\ \times \exp\left(i \, \vec{k} \cdot \vec{r} \right) N(\xi) {}_1F_1 \\ \times \left(-i\,\xi; \, 1; \, -i\,k\,r - i\,\vec{k} \cdot \vec{r} \right) \end{aligned} \tag{10}$$

with $\xi = Z_T^*/k$. The effective nuclear charge of the residual target, Z_T^*, is defined following the same criteria employed by Belkić for electron capture [45], namely $Z_T^* = \sqrt{-2\, n_i^2 \, \varepsilon_i}$, where n_i is the principal quantum number of each atomic orbital that constitutes the initial bound state of the active electron, and ε_i the corresponding orbital energy.

The cross sections are then obtained by numerically integrating the transition amplitude (3) using the well known QUADPACK integration routines [46]. Moreover, in order to calculate the resulting hypergeometric functions appearing in the transition amplitude, in the cases where the Sommerfeld parameters are larger than unity, transformation formulae are used to achieve convergence conditions [47].

4. Results and discussions

4.1. Energy distribution of DDCS

In figure 1, the energy distribution of DDCS for Ne is shown for different observation angles. In each plot the solid line refers to the total DDCS values obtained from the CDW-EIS calculations. The other curves correspond to the contributions from different sub-shells. Similar plots for the Xe target are displayed in figure 2 without the sub-shell contributions. Due to the large number of sub-shells involved, these contributions are shown separately in figure 3 for three representative angles.

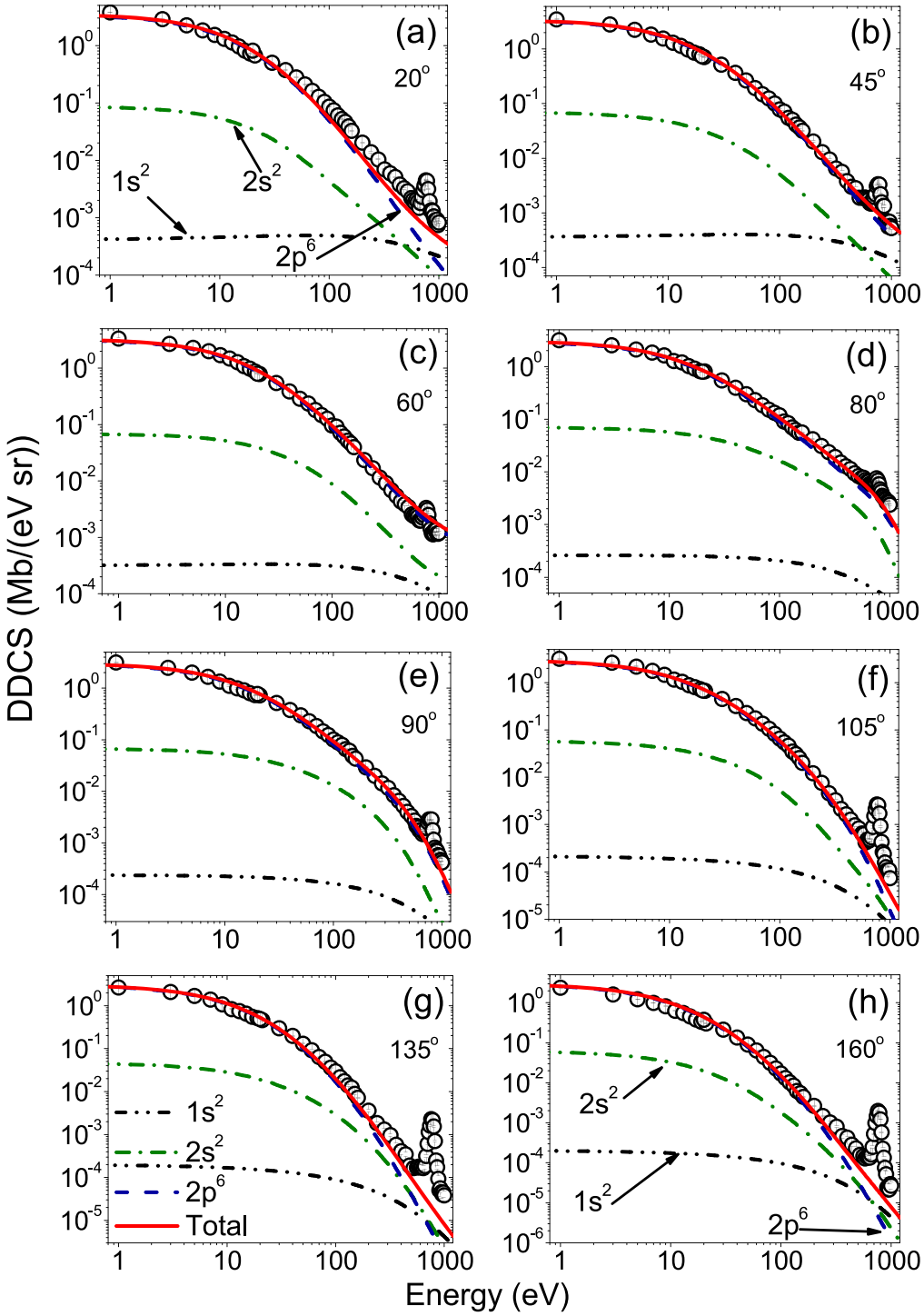

Figure 1. Energy distribution of the absolute electron DDCS for Ne. The solid line in each plot corresponds to the total DDCS obtained from the CDW-EIS model. The other curves represent different sub-shell contributions.

In the case of Ne (figure 1), the DDCS falls off rapidly with increasing electron energy. In the low energy region, where the cross section reaches its maximum, the involved momentum transfer from the projectile to the active electron is very small like in a dipolar transition. These low energy electrons are mainly produced in large impact parameter collisions. For electrons emitted with higher energy, more penetrating collisions, which correspond to small impact parameters, are necessary. However, the probability for collisions at these low impact parameters diminishes. As a result, with increasing energy the cross section decreases. In the extreme higher energy region, in each plot, a broad peak at around 780 eV exists. This is the K-LL Auger electron emission peak for Ne. The broadness of the peak is due to the contributions from multiple Auger satellite lines, whose energy separation comes within the energy resolution of the

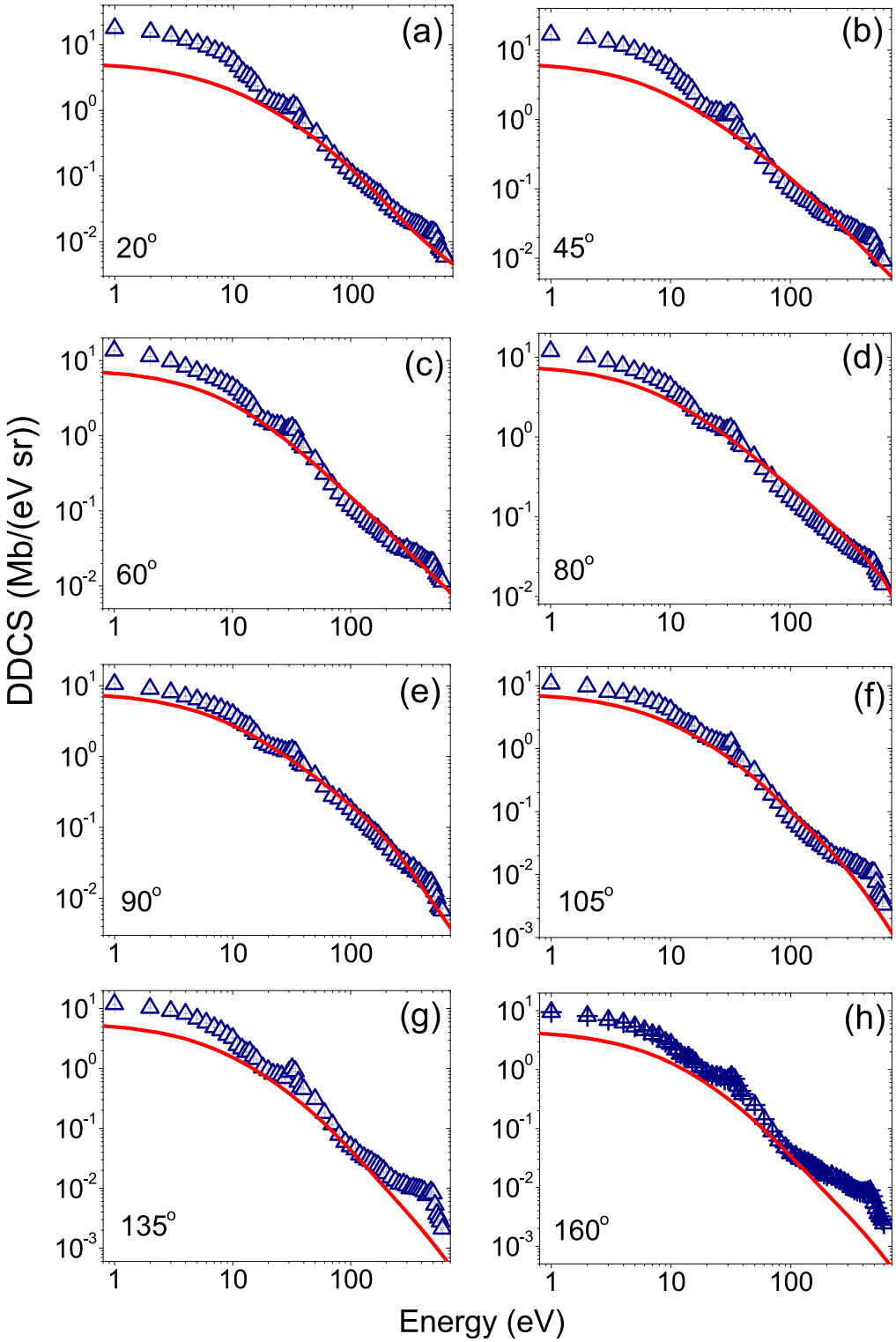

Figure 2. Energy distribution of the absolute electron DDCS for Xe. The solid line in each plot corresponds to the total DDCS obtained from the CDW-EIS model.

spectrometer. Different L-subshell vacancies during the relaxation process give rise to these satellite lines. It can be noted that the Auger peak is much more prominent at the backward angles relative to the forward and the intermediate angles. This is because the cross section of the Coulomb ionization continuum is relatively larger at the forward and the intermediate angles. As a result, at these angles, it obscures the Auger peak to some extent.

In the plots, we also provide a comparison between the experimental data and the theoretical prediction (solid line), namely, the *prior* form of the CDW-EIS calculation. In general, an overall very good qualitative agreement has been

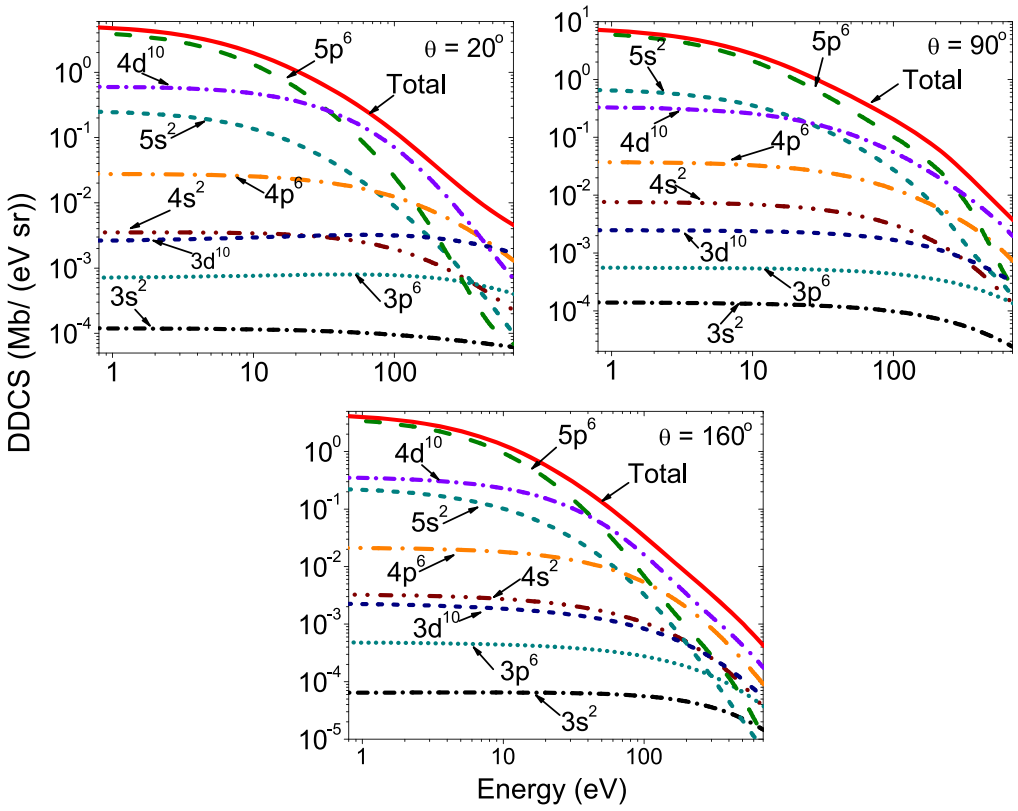

Figure 3. Energy distribution of the absolute DDCS corresponding to different sub-shell contributions for Xe.

achieved for all angles. Now, as far as absolute values are concerned, in the low energy region the calculation reproduces the experimental observations reasonably well for all angles. It also provides very good agreement at the intermediate angles for the entire energy range. But, the agreement is a little worse in the higher energy range ($\gtrsim$100 eV), particularly for the extreme forward and backward angles. The calculated DDCS values slightly underestimate the experimentally observed values. It would be appropriate to mention here that this overall good agreement with the Coulomb ionization continuum spectra is due to the fact that the *prior* form of the model efficiently incorporates the target passive electron dynamical screening effect on the evolution of the active electron, for this kind of system. But, as this model does not incorporate any characteristic relaxation process, it does not show the Auger peak. It only describes the direct Coulomb ionization processes. Now, coming to the discussion of different sub-shell contributions, estimated in this theoretical framework, it is seen that, for all angles, in the low energy region, the outer most sub-shell i.e. $2p^6$ is the main contributor to the total DDCS. $2s^2$ and $1s^2$ are about one and four orders of magnitude lower than this, respectively. As electron energy increases, the inner sub-shell contributions also become comparable to the outer sub-shell. Even after a certain energy, the inner sub-shell dominates over the outer sub-shell. It is clearly visible for the cases of the backward angles. This behaviour could be attributed to the fact that at this high energy emission (small impact parameters) the projectile has a larger probability of finding inner sub-shell electrons, and at the same time they move with higher velocity in their initial state, facilitating thus the momentum transfer.

In the case of Xe (figure 2), the energy distribution spectra of the DDCS are not as smooth as that of the Ne. In the very low energy region, the DDCS smoothly decreases with electron energy, similar to the case of Ne. But after that it forms a small broad peak-like structure at around 32 eV. Earlier, it has been identified as an admixture of different N-OO Auger lines [48]. These lines are situated within 18 eV and 38 eV, though the main intense lines are within 29 eV and 35 eV. Within that region, some other auto-ionization lines also exist. Thereafter, the DDCS spectrum again falls off with electron energy until it encounters another Auger electron emission peak at around 480 eV. This consists mainly of different M-NN Auger transition lines. According to [48], these lines are scattered in the energy region between 350 eV and 550 eV. But the main intense groups are within 520 eV and 550 eV. Therefore, the present observation of Auger peak position is slightly left-shifted. There are also some other low intensity M-NO Auger lines within the energy region between 560 eV and 600 eV. These all together form the experimentally observed hump-like structure.

In the present case, in general, the agreement between the CDW-EIS calculation and the experimental data is relatively poor compared to the case of the Ne. At the forward angles, in the low energy region, the theoretical prediction underestimates the experimental DDCS. In the higher energy region the agreement is better, relatively. At intermediate angles, the

overall agreement is much better compared to the other angles. Here, in the low energy part the discrepancy between the theory and the experimental data is also much smaller. On the other hand, at the extreme backward angles, the theory again underestimates the experimental findings in the low energy region as well as in the very high energy region. In the intermediate energy region, the agreement is good to some extent. This overall lack of agreement between the theory and the experiment can be due to several facts. In this case, the DDCS spectrum, in the detected energy range, is influenced considerably by different Auger relaxation processes, whose descriptions are out of the scope of this theoretical model. It should also be noted that, unlike Ne for this kind of large atom, collective multi-electron dynamics give rise to giant resonances which can exhaust the single particle excitations. For Xe, the collective resonance, namely the shape resonance, has been seen around 100 eV with a width of about 40 eV [49, 50]. However, the ionized electrons following the decay of the collective state will fall at the low energy part of the spectrum, i.e. the kinetic energy of the ionized electron would be $\varepsilon_e = E_{CE} - I_p$, where E_{CE} and I_p are the collective excitation energy and ionization potential of that electron, respectively. Now, if we look at different sub-shell contributions, plotted in figure 3, for all angles, in the low energy region, the outer most sub-shell i.e. $5p^6$ contributes the most. Similar to the case of the Ne, here also, as energy increases the other sub-shell contributions come into picture. At the extreme forward and the backward angles, after certain tens of eV the $4d^{10}$ sub-shell starts dominating the others. On the other hand, for an intermediate angle, the crossover between $5p^6$ and $4d^{10}$ occurs at a much larger energy value. Close to the 90° emission angle, binary-encounter collisions contribute to the DDCS, facilitating the ejection of less bound sub-shells. This probably explains the dominance of emission from $5p^6$ and $5s^2$ over $4d^{10}$, which is extended to larger electron energies up to 300 eV, even considering that a larger amount of electrons occupy the $4d$ orbital. This is in contrast to forward and backward emission which is dominated by dipolar transitions at low electron energies. At much higher energies, for all angles, other highly filled inner sub-shells like $4p^6$ contribute considerably. In general, the outer sub-shell DDCS falls off much more rapidly with electron energy compared to that of the inner sub-shells.

4.2. Angular distribution of DDCS

In figure 4, the angular distributions of the DDCS, at different electron energies, for the Ne target are plotted. The solid lines in each of the plots denote the total DDCS values obtained from the CDW-EIS calculations and the other curves represent the angular distributions of the sub-shell contributions. It can be seen that, at the lowest detected energy i.e. 1 eV, the angular distribution is nearly flat with a slight negative slope. With increasing electron energy, the shape of the angular distributions gradually changes. It takes a broad bump-like structure with the maxima at around 80°. This change takes place right from ∼20 eV (not shown). But from 50 eV onwards, it is more clearly visible. At energies around 100 eV and higher, the peak becomes quite sharp. This increase in cross section at the intermediate angles was explained earlier as caused by the binary encounter (BE)-type collision between projectile nucleus and 'almost free' electrons [1]. The other notable aspect is that, at higher energies, the angular distributions are not symmetric about the peak. The forward angle DDCS values are much higher than the backward angle DDCS values. For example, at 520 eV, the ratio of the DDCSs at 20° and at 160° is about 18.0. On the other hand, this asymmetry is not so large for lower energies, like for 1 eV or 11 eV the above-mentioned ratio values are about 1.6 and 2.1, respectively. Furthermore, the forward–backward angular asymmetry increases gradually with electron energy. This kind of asymmetric angular distribution in the case of ion–atom collision can be explained by means of the two centre electron emission (TCEE) process [51–53]. Subsequent to the ionization process, the ejected electrons move in an electric field produced by both the residual target as well as the projectile. Due to the Coulomb field of the forward-moving ionic projectile, the electrons are attracted in the forward direction causing the higher cross section in the forward direction compared to the backward direction.

Now as far as theoretical prediction is concerned, up to 50 eV, the absolute agreement with the experimental data is very good. After that, though the absolute agreement is not that good, particularly at the extreme forward and backward angles, the essential qualitative features of the data are reproduced well by the theory. In fact, at intermediate angles the absolute agreement is also very good, where the collision dynamics is mostly dominated by the BE process. At the extreme forward and backward angles, the CDW-EIS calculation underestimates the experimental findings. This deviation slightly increases gradually with increasing electron energy. As explained, for these cases, the collision dynamics is mostly dominated by 3-body processes in which the two centre effect (TCE) is quite active. In this case, at the lower energies up to about 50 eV, $2p^6$ is a much more dominant contributor to the total DDCS (in fact, for 1 eV and 11 eV plots, the $2p^6$ DDCS curve (dashed line) is behind the total DDCS curve (solid line)). At higher energies, particularly at extreme backward angles, the $2s^2$ sub-shell competes well with the $2p^6$ sub-shell. In fact, at 520 eV, after 120° the contributions from these two sub-shells are very nearly equal. In general, one notable fact is that the $2p^6$ and the $2s^2$ sub-shell exhibit a BE peak-like structure similar to the experimental data, but the inner most sub-shell i.e. $1s^2$ does not show that kind of structure. Its contribution gradually decreases with increasing angle and after 120° it almost saturates. This may be due to the fact that the $1s^2$ electrons are not as 'free' as the loosely bound outer shell electrons. In fact, ionization for this inner sub-shell cannot be considered as a simple binary encounter with the projectile. The other reason could be the wide velocity distribution of these electrons, which would tend to spread out and lower the peak.

In figure 5, similar angular distributions are plotted for the Xe target. For comparison, in the same plots we also provide the Ne data (circles joined by lines) of corresponding

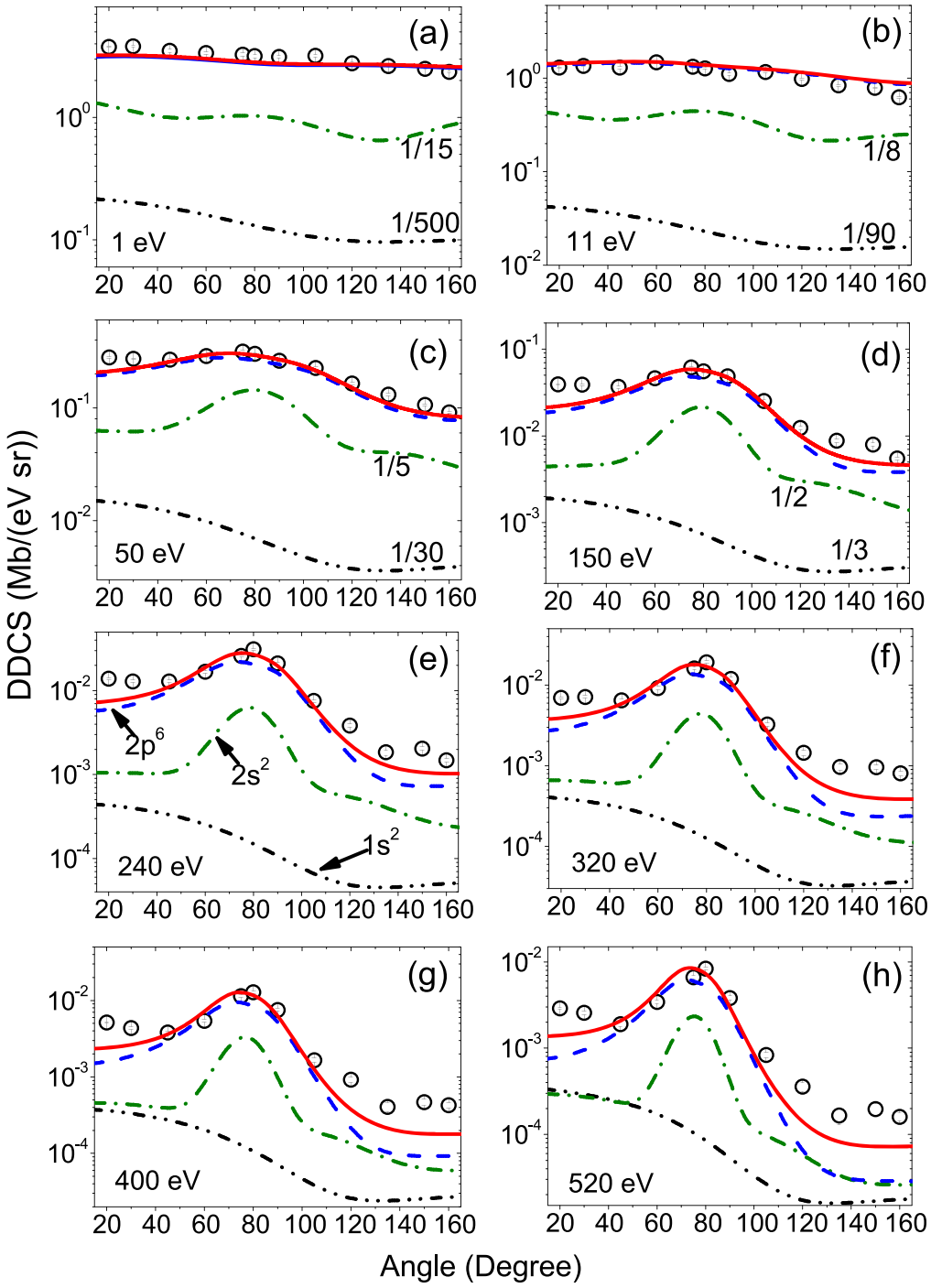

Figure 4. Angular distribution of the absolute electron DDCS for Ne. The solid line in each plot corresponds to the total DDCS obtained from the CDW-EIS model. The other curves represent different sub-shell contributions. The fractional number adjacent to some curves has to be multiplied with the vertical scale to obtain respective absolute cross section.

energy. Here the electron energies are chosen such that these do not belong to the Auger regions. But, apart from the fact that the Ne DDCS distribution is always lower than that of the Xe, one does however see that the overall qualitative features of the Xe distributions are to some extent different from that of the Ne. At 1 eV, it has a small dip at the intermediate angular region, whereas for Ne, as mentioned earlier, it is an almost flat distribution. At 11 eV, unlike the Ne data, no prominent BE signature is present. At the higher energies, 70 eV onwards, the BE electron emission signature is visible at the intermediate angles. The other notable fact is that, in this case, the forward–backward asymmetry is much lower compared to the case of Ne. For example, at 120 eV the ratio of the extreme forward angle DDCS to that of the extreme backward angle is about 2.8 for Xe, whereas for Ne this value is about 6.0. At 320 eV, the same ratio values are about 1.9 and 8.6 for Xe and Ne, respectively. In fact, seeing these two exemplary energies, unlike Ne, the forward–backward

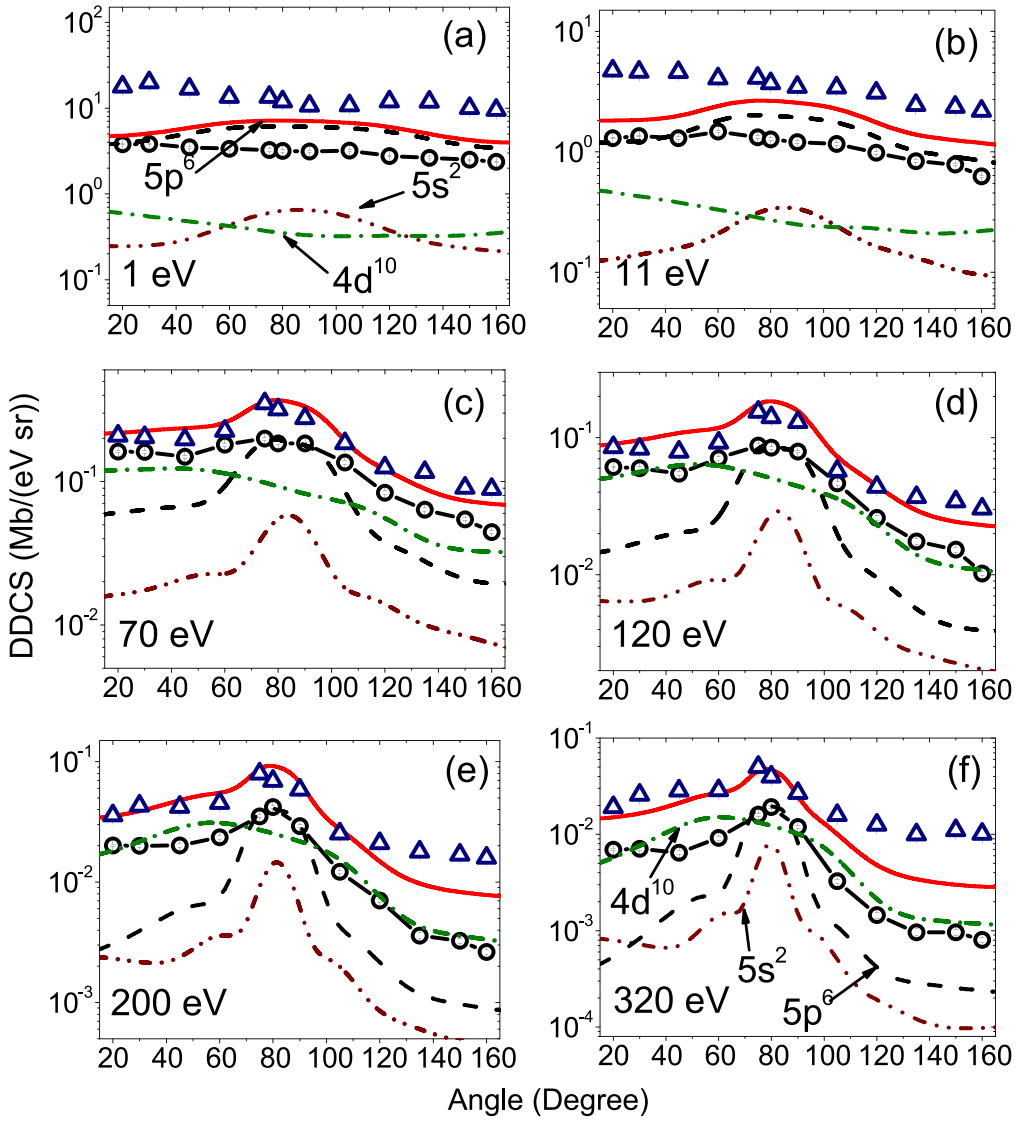

Figure 5. Angular distribution of the absolute electron DDCS for Xe (triangle). The circles joined by lines represent the similar distribution for Ne. The solid line in each plot corresponds to the total DDCS obtained from the CDW-EIS model for Xe. The other curves represent different sub-shell contributions for Xe.

asymmetry slightly decreased with increasing energy. Therefore, one can see that the nature of the angular distribution for the Xe target is a bit different from that of the Ne target.

In this case, as seen before, the overall agreement between the theoretical calculation and the experimental data is not as satisfactory as the case for Ne. At lower energies such as 1 eV or 11 eV, the CDW-EIS calculation predicts a small hump-like structure, with which the experimental data do not agree, particularly at the extreme angles. Compared to the lower energy part, the qualitative agreement in the intermediate energy region at e.g. 70 eV or 120 eV is much better. In cases of even higher energies, the theory reproduces the data at the forward and the intermediate angles quite well. However it underestimates the cross section at the backward angles, i.e. it predicts larger forward–backward angular asymmetry than that shown by the experimental data. Now, as far as individual sub-shell contribution is concerned (in the plotted energy range, $5p^6$, $5s^2$ and $4d^{10}$ are the main contributors to the total DDCS, other are comparatively smaller in magnitude), in the lower energies the $5p^6$ sub-shell governs the overall feature. But in the intermediate energy range from about 50 eV onwards, the $4d^{10}$ sub-shell dominates at the forward and the backward angles and the $5p^6$ sub-shell contributes the most at the intermediate angular region. At very high energies, the maximum part of the angular distribution is dominated by the contribution from the $4d^{10}$ sub-shell. In general, if we look at the shape of the curves, in the low energy region, the $5p^6$ and the $5s^2$ have a broad hump-like structure, whereas the $4d^{10}$ has a minima at the intermediate angular region. As electron energy increases, the first two show a very sharp peak structure at the intermediate angular region, but the $4d^{10}$ sub-shell shows a relatively much broader hump structure. This may be the reason behind the fact that, at the higher energies, the BE peak in this case is not as sharp as that of the Ne.

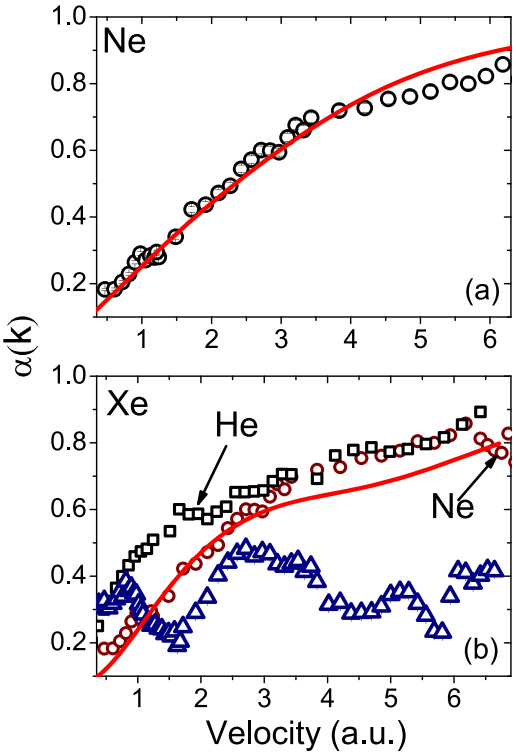

Figure 6. Velocity distribution of the asymmetry parameter for (a) Ne and (b) Xe. The solid lines correspond to the theoretical calculations based on the CDW-EIS model. In the plot (b), the squares and the circles represent similar distributions for He (6 MeV u^{-1} C^{6+} impact) [29] and Ne, respectively.

4.3. Angular asymmetry parameter

We have seen in the above section that there is a forward–backward angular asymmetry involved with the electron emission process. The amount of asymmetry varies with electron energy (ε_e). The asymmetric nature of the electron angular distribution is caused by the TCE as well as the non-Coulomb nature of the target potential for large multi-electronic systems. To have a quantitative estimate, the angular asymmetry parameter $\alpha(k)$ can be defined as [23],

$$\alpha(k, \theta) = \frac{\sigma(k, \theta) - \sigma(k, \pi - \theta)}{\sigma(k, \theta) + \sigma(k, \pi - \theta)} \qquad (11)$$

where electron energy $\varepsilon_k = \frac{k^2}{2}$ (a.u.) and θ is a forward angle. In principle θ should be 0°, but since the DDCS shows a flat distribution near 0° and 180°, we choose $\theta = 30°$. Then also the derived $\alpha(k)$ would serve as the measure of forward–backward angular asymmetry.

In figure 6, the electron velocity (v) distributions of $\alpha(k)$ are shown for Ne (a) and Xe (b). The corresponding CDW-EIS predictions are denoted by the solid line. In the case of Ne, the $\alpha(k)$ takes a very low value, around 0.15, at low velocity. Thereafter, it increases monotonically with increasing electron velocity. At around $v \backsim 6$ a.u., i.e. $\varepsilon_e \backsim 500$ eV, the $\alpha(k)$ value is about 0.85. According to the definition, a higher $\alpha(k)$ value corresponds to more asymmetric electron emission. Therefore, the values suggest that for the low energy electron emission, the amount of forward–backward angular asymmetry is much less and as electron energy increases the asymmetry parameter increases monotonically. This is also evident from the DDCS angular distribution plots. This happens because the higher energy electrons have a velocity relatively close to the velocity of the projectile. These electrons are much more affected by the projectile Coulomb field compared to the lower energy electrons. Similar qualitative behaviour was seen earlier for the He target [8, 29]. Now, it is seen from the present plot that the CDW-EIS calculation reproduces the entire distribution quite well. Though there is a slight mismatch on the higher velocity side, overall it can be claimed that the agreement between the calculation and the experimental observation is very good. At this point, it is worth mentioning that it was realized earlier that the other non-distorted perturbative models such as first-order Born calculations do not give as good a result as that obtained in the present case [1, 2, 6, 8]. The reason behind this good result can be identified as the proper inclusion of the projectile Coulomb field effect in the initial as well as in the final channels of the collision process.

Now if we look at a similar plot for Xe (b), we find that the qualitative features of the distribution are completely different from that of the Ne or He (6 MeV u^{-1} C^{6+} impact on He; data is taken from [29]). But in this case, unlike Ne, the plotted velocity range includes the Auger regions. In the lower velocity region, the $\alpha(k)$ starts from a slightly higher value compared to the Ne. But after about $v = 1$ a.u., the value starts decreasing with increasing electron velocity until about $v \backsim 1.6$ a.u. This region can be identified as the N-OO Auger region. After that it increases up to the value of about 0.5 corresponding to $v \backsim 3.0$ a.u. Then it again decreases discontinuously until it encounters a minima at around $v \backsim 5.8$ a.u. This region can also be identified as the Auger region consisting of M-NN and M-NO lines. Overall, within the entire velocity range, the $\alpha(k)$ value does not exceed the value 0.5, which is much less compared to the maximum value for the Ne or the He. Behind this very different behaviour, the non-Coulomb potential for such a large atom must play a role. In the present case, the CDW-EIS calculation fails to reproduce the observed behaviour. It shows a nearly monotonically increasing behaviour similar to the case of the Ne. This disagreement may be due to the presence of different Auger channels whose nature of angular asymmetry is completely different from that of the direct Coulomb ionization case.

4.4. Single differential cross section (SDCS) and total cross section (TCS)

To understand the overall energy and angular distributions of the electron emission, we have derived the SDCS by integrating the DDCS spectra. In figure 7(a), the energy distributions of the SDCS, which is obtained by integrating the DDCS over the entire angular range, are plotted for Ne (circle) and Xe (triangle). Similarly in figure 7(b), the angular distributions of the SDCS, obtained by integrating the DDCS over the detected electron energy range, are plotted for Ne (circles) and Xe (triangles). In both the plots, the solid line

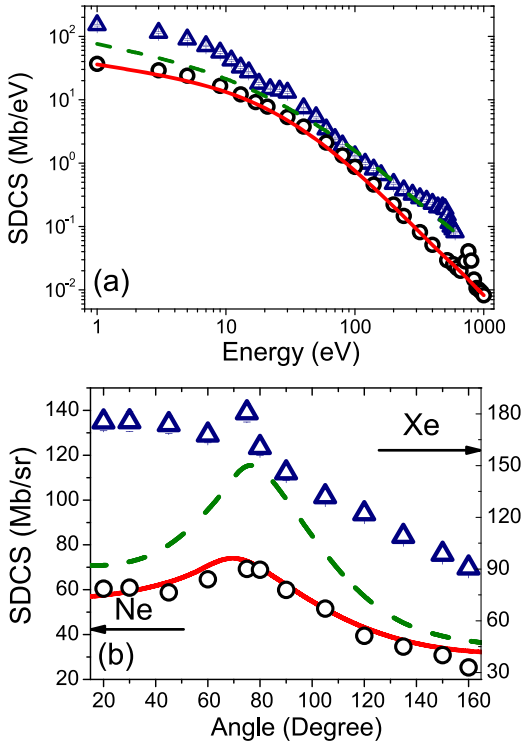

Figure 7. Energy (a) and angular (b) distributions of the absolute electron SDCS for Ne (circles) and Xe (triangles). The solid line and the dashed line correspond to the CDW-EIS calculation for the Ne and the Xe, respectively. In plot (b), the left and the right vertical scale correspond to the Ne and the Xe targets, respectively.

denotes the CDW-EIS predictions for Ne and the dashed line represents the predictions for Xe. The qualitative behaviour of the energy distributions, for both the targets, is very similar to that of the respective DDCS distributions. All the Auger peaks are also clearly visible in the SDCS level. In case of Ne, the agreement between theory and experiment is very good. On the other hand, for Xe, though the agreement is good in the higher energy region, the theory underestimates the experimental ones in the lower energy region. If a comparison between Ne and Xe data is carried out, one can note that for the entire energy range the Xe SDCS is higher than Ne SDCS, except around 100 eV. In that region both the SDCSs are very close to each other.

In the angular distribution plots, the agreement between the theory and the experiment, for the Ne, is quite good. It excellently reproduces all the qualitative features. On the contrary, for the Xe, the theory underestimates the experimental data at the forward and the backward angles by a factor of almost 2.0. The theory predicts a sharp BE peak at the intermediate angle, whereas the experimental data shows almost no signature of peak except a higher cross section point at 75°.

The total cross section (TCS) is also obtained for both cases by integrating the SDCS spectrum. In the case of Ne, the experimentally obtained TCS is 630 Mb, whereas for Xe, it is 1702 Mb. So the Xe TCS is about 2.7 times higher than the Ne TCS. The CDW-EIS model predicted TCS values are 663 Mb and 1265 Mb for Ne and Xe, respectively. It is interesting to note that the Xe mean size is a factor 2.8 larger than the Ne one, containing more outer electrons with smaller binding energies.

5. Conclusions

In conclusion, we have studied the double differential cross section of electron emission from Ne and Xe atoms under the impact of fast bare carbon ions of energy 5 MeV u^{-1}. The study aimed to understand the electron emission process in the case of large multi-electronic systems. It has been noted that there are several differences between the electron emission processes corresponding to Ne and Xe. Unlike Ne, the DDCS spectrum for Xe is dominated by different Auger transitions right from the low energy region. The qualitative features of the electron angular distributions, corresponding to the non-Auger electron energy region, for Xe, is also quite different from that of the Ne. For example, the sharp peak due to binary encounter collision in the higher electron energy region, which is very prominent in case of the Ne, almost vanishes for the Xe target. Moreover, the forward–backward asymmetry is quite low even for higher energy electrons for the Xe compared to the Ne. This is clearly shown in the velocity distribution plot of the angular asymmetry parameter. The angular asymmetry parameter for Xe does not show a monotonically increasing behaviour with electron velocity like Ne or He. We have also carried out the theoretical calculations based on the *prior* form of the CDW-EIS model for both the targets. Within this framework, the contributions from different sub-shells are estimated. In general, the model is more or less successful in reproducing the experimental findings for Ne. There are some disagreements between the theory and the experiment in the higher electron energy region, particularly at extreme forward and backward angles. It is also able to reproduce the observed forward–backward asymmetry in the angular distribution very well throughout the entire electron energy range. The energy as well as the angular dependence of the derived SDCS also agree very well with the CDW-EIS prediction. In this case, the main contribution to the total DDCS comes from the outermost sub-shell for most of the energy region. For higher energy electron emission at backward angles, the inner sub-shell contributions come into the picture. In the case of the Xe target, the overall agreement between the theory and the experimental data is not as good as that for the Ne. In the low energy part of the spectrum the theory underestimates the data, but at the intermediate angular region the agreement is much better. The theory also overestimates the observed forward–backward angular asymmetry. This overall lack of agreement may be due to the presence of different Auger relaxation processes and also the collective excitation mechanism, which are not included in the theoretical model. In this case, for the lower energy electron emission, the $5p^6$ sub-shell is the main contributor to the total DDCS. As energy increases the $4p^{10}$ sub-shell becomes the main one for most of the emission angles, except the intermediate region where the $5p^6$ sub-shell dominates. The dominance of the $4p^{10}$ sub-shell contribution in

the higher energy range can be identified as the cause of the smearing out of the BE peak. It is hard to consider ionization of these tightly bound inner shell electrons as a simple binary encounter with the projectile. We have also estimated the total ionization cross section for both the targets. For the Ne target, the theory is a little higher than the experimentally observed value. On the other hand, for Xe, it underestimates by a factor of about 1.3. Overall, the study suggests that because of the big difference in target electron numbers, the descriptions of the electron emission processes for Ne and Xe targets are considerably different, and though the theoretical description for multi-electronic systems like Ne is nearly adequate, for relatively large multi-electronic systems like Xe, there are other mechanisms to be included in the framework for completeness—considering, for example, collective effects and improving the description of the continuum wavefunction for the different sub-shells.

Acknowledgments

The authors would like to thank the Pelletron accelerator team for smooth operation of the machine and Nilesh Mhatre for his help during the experiment. JMM and RDR acnowledge finantial support from the Agencia Nacional de Promoción Científica y Tecnológica of Argentina through the project PICT 2011–2145.

References

[1] Manson S T, Toburen L H and Stolterfoht N 1975 *Phys. Rev.* A **12** 60
[2] Stolterfoht N, Platten H, Schiwietz G, Schneider D, Gulys L, Fainstein P D and Salin A 1995 *Phys. Rev.* A **52** 3796
[3] Tribedi L C, Richard P, DeHaven W, Gulýas L, Gealy M W and Rudd M E 1998 *J. Phys. B: At. Mol. Opt. Phys* **31** L369
[4] Tribedi L C, Richard P, Wang Y D, Lin C D, Gulýas L and Rudd M E 1998 *Phys. Rev.* A **58** 3619
[5] Tribedi L C, Richard P, Wang Y D, Lin C D, Olson R E and Gulýas L 1998 *Phys. Rev.* A **58** 3626
[6] Tribedi L C, Richard P, Gulýas L and Rudd M E 2001 *Phys. Rev.* A **63** 062724
[7] Jana S, Samanta R and Purkait M 2012 *Eur. Phys. J.* D **66** 243
[8] Misra D, Kelkar A H, Fainstein P D and Tribedi L C 2012 *J. Phys. B: At. Mol. Opt. Phys* **45** 225201
[9] Stolterfoht N *et al* 2001 *Phys. Rev. Lett.* **87** 023201
[10] Misra D, Kadhane U, Singh Y P, Tribedi L C, Fainstein P D and Richard P 2004 *Phys. Rev. Lett.* **92** 153201
[11] Tanis J A, Hossain S, Sulik B and Stolterfoht N 2005 *Phys. Rev. Lett.* **95** 079301
[12] Misra D, Kadhane U, Singh Y P, Tribedi L C, Fainstein P D and Richard P 2005 *Phys. Rev. Lett.* **95** 079302
[13] Misra D, Kelkar A, Kadhane U, Kumar A, Fainstein P D and Tribedi L C 2006 *Phys. Rev.* A **74** 060701
[14] Winkworth M, Fainstein P D, Galassi M E, Baran J, Dassanayake B S, Das S, Kayani A and Tanis J A 2009 *Nucl. Ins. Meth. Phy. Res. B* **267** 373
[15] Nandi S, Agnihotri A N, Kasthurirangan S, Kumar A, Tachino C A, Rivarola R D, Martin F and Tribedi L C 2012 *Phys. Rev.* A **85** 062705
[16] Kelkar A H, Kadhane U, Misra D, Gulyas L and Tribedi L C 2010 *Phys. Rev.* A **82** 043201
[17] Moretto-Capelle P and Padellec A L 2006 *Phys. Rev.* A **74** 062705
[18] Tribedi L C, Agnihotri A N, Galassi M E, Rivarola R D and Champion C 2012 *Eur. Phys. J.* D **66** 303
[19] Agnihotri A N, Nandi S, Kasthurirangan S, Kumar A, Galassi M E, Rivarola R D, Champion C and Tribedi L C 2013 *Phys. Rev.* A **87** 032716
[20] Nandi S, Biswas S, Khan A, Monti J M, Tachino C A, Rivarola R D, Misra D and Tribedi L C 2013 *Phys. Rev.* A **87** 052710
[21] Montenegro E C, Sigaud G M and DuBois R D 2013 *Phys. Rev.* A **87** 012706
[22] Fainstein P D, Ponce V H and Rivarola R D 1988 *J. Phys. B: At. Mol. Opt. Phys* **21** 287
[23] Fainstein P D, Gulyás L, Martín F and Salin A 1996 *Phys. Rev.* A **53** 3243
[24] Misra D, Kelkar A H, Fainstein P D and Tribedi L C 2007 *J. Phys.: Conf. Ser.* 80 012013
[25] Misra D, Kelkar A H, Kadhane U, Kumar A, Singh Y P, Tribedi L C and Fainstein P D 2007 *Phys. Rev.* A **75** 052712
[26] Crothers D S F and McCann J F 1983 *J. Phys. B: At. Mol. Opt. Phys.* **16** 3229
[27] Monti J M, Fojón O A, Hanssen J and Rivarola R D 2010 *J. Phys. B: At. Mol. Phys.* **43** 205203
[28] Monti J M, Fojón O A, Hanssen J and Rivarola R D 2010 *J. At. Mol. Opt. Phys* **2010** 1
[29] Biswas S, Misra D, Monti J M, Tachino C A, Rivarola R D and Tribedi L C 2014 *Phys. Rev.* A **90** 052714
[30] Tribedi L C and Tandon P N 1992 *Nucl. Ins. Meth. Phy. Res.* B **69** 178
[31] Kasthurirangan S *et al* 2013 *Phys. Rev. Lett.* **111** 243201
[32] Tribedi L C, Nanal V, Press M R, Kurup M B, Prasad K G and Tandon P N 1994 *Phys. Rev.* A **49** 374
[33] Tribedi L C, Nanal V, Kurup M B, Prasad K G and Tandon P N 1994 *Phys. Rev.* A **51** 1312
[34] Cacak R K and Jorgensen T Jr 1970 *Phys. Rev.* A **2** 1322
[35] Crooks J B and Rudd M E 1971 *Phys. Rev.* A **3** 1628
[36] Woerleet P H, Gordeev Y S, Waard H de and Saris F W 1981 *J. Phys. B: At. Mol. Opt. Phys* **14** 527
[37] Bernardit G, Fainstein P, Garibottii C R and Suárez S 1990 *J. Phys. B: At. Mol. Opt. Phys.* **23** L139
[38] Gay T J, Gealy M W and Rudd M E 1990 *J. Phys. B: At. Mol. Opt. Phys* **23** L823
[39] DuBois R D and Manson S T 1990 *Phys. Rev.* A **42** 1222
[40] Suaŕez S, Garibotti C, Meckbach W and Bernardi G 1993 *Phys. Rev. Lett.* **70** 418
[41] Suaŕez S, Garibotti C, Bernardi G, Focke P and Meckbach W 1993 *Phys. Rev.* A **48** 4339
[42] Kuzel M, DuBois R D, Maier R, Heil O, Jakubassa-Amundsen D H, Lucas M W and Groeneveld K O 1994 *J. Phys. B: At. Mol. Opt. Phys* **27** 1993
[43] Misra D, Thulasiram K V, Fernandes W, Kelkar A H, Kadhane U, Kumar A, Singh Y P, Gulyas L and Tribedi L C 2009 *Nucl. Ins. Meth. Phy. Res.* B **267** 157
[44] Clementi C and Roetti C 1974 *At. Data Nucl. Data Tables* **14** 177
[45] Belkić D 1978 *J. Phys. B: At. Mol. Phys.* **11** 3529
[46] Piessens R, Doncker-Kapenga E De and Überhuber C W 1983 *QUADPACK: a Subroutine Package for Automatic Integration* (Berlin: Springer) ISBN: 3–540-12553–1 http://nines.cs.kuleuven.be/software/QUADPACK/
[47] Stegun M and Abramowitz I 1970 *Handbook of Mathematical Functions* (New York: Dover)

[48] Werme L O, Bergmark T and Siegbahn K 1972 *Phys. Scr.* **6** 141
[49] Ederer D L 1964 *Phys. Rev. Lett.* **13** 760
[50] Becker U, Prescher T, Schmidt E, Sonntag B and Wetzel H E 1986 *Phys. Rev.* A **33** 3891
[51] Stolterfoht N *et al* 1987 *Europhys. Lett.* **4** 899
[52] Fainstein P D, Ponce V H and Rivarola R D 1991 *J. Phys. B: At. Mol. Phys.* **24** 3091
[53] Stolterfoht N, DuBois R D and Rivarola R D 1997 *Springer Series of Atoms and Plasmas* vol 20 (Berlin: Springer) ISBN 3–540-63184–4